JOURNAL OF MATERIALS SCIENCE 29 (1994) 2884–2892

Structure and decomposition behaviour of rapidly solidified Al–Fe alloys

D. H. KIM
Center for Advanced Aerospace Materials, Department of Material Science and Metallurgical Engineering, Pohang Institute of Science and Technology, P.O. Box 125, Pohang, Kyungbuk, 790 600, Korea

B. CANTOR
Oxford Centre for Advanced Materials and Composites, Department of Materials, Oxford University, Parks Road, Oxford OX1 3PH, UK

The structure and decomposition behaviour of rapidly solidified Al–5, 10 and 15 at % Fe alloys have been investigated by detailed transmission electron microscopy and differential scanning calorimetry. Rapid solidification produces a variety of metastable phases: microquasicrystalline, decagonal, Al_mFe, Al_6Fe and $Al_{13}Fe_4$, in order of increasing thermodynamic stability. The rapidly solidified microstructure depends upon the alloy composition and cooling rate. Primary and cellular particles of the microquasicrystalline phase are preferred at higher cooling rates, and primary or eutectic particles of the Al_mFe phase are preferred at lower cooling rates. With increasing iron content, the microquasicrystalline phase is replaced with primary particles of the decagonal phase. After annealing at moderate temperatures, the microquasicrystalline phase in Al–5 and 10 at % Fe decomposes into Al_mFe and Al_6Fe, and the microquasicrystalline phase in Al–15 at % Fe decomposes into Al_mFe. After annealing at higher temperatures, the Al_mFe, Al_6Fe and decagonal phases then decompose into stable $Al_{13}Fe_4$.

1. Introduction

Rapidly solidified Al–Fe alloys have been studied extensively because of their potential applications in high-temperature aerospace components [1, 2]. Various types of microstructure are found in rapidly solidified Al–Fe alloys depending upon the alloy composition and cooling rate, with a range of different metastable phases such as the icosahedral phase, decagonal phase, Al_mFe, Al_6Fe and Al_xFe, as well as the stable phase $Al_{13}Fe_4$ [1–8].

There has been a wide variety of different reports about the as-rapidly solidified microstructure and subsequent decomposition behaviour of rapidly solidified Al–Fe alloys. For example, the microstructure of hypereutectic Al–Fe alloys with less than 5 at % Fe have been reported to consist of different combinations of primary α-Al, primary $Al_{13}Fe_4$, eutectic α-Al and Al_6Fe, and a fine-scale cellular network, depending upon the cooling rate [1, 2, 9–11]. On the other hand, hypereutectic Al–Fe alloys with greater than 5 at % Fe have been reported to consist of different combinations of α-Al, primary $Al_{13}Fe_4$, primary icosahedral phase, primary Al_mFe, and a fine-scale cellular network of α-Al and Al_mFe or the icosahedral phase, again depending upon the cooling rate [7, 8].

The present paper describes a study of the solidification microstructure and decomposition behaviour of rapidly solidified Al–Fe alloys as a function of alloy composition and cooling rate.

2. Experimental procedure

The Al–Fe alloys were prepared by induction melting high-purity aluminium and iron in recrystallized alumina crucibles under a dynamic argon gas atmosphere. Nominal alloy compositions were Al–5, 10 and 15 at % Fe. Actual compositions were determined in a Cameca Camebax wavelength dispersive X-ray microprobe analyser and were found to be Al–5.13, 9.63 and 14.92 at % Fe, respectively.

Specimens from each alloy were rapidly solidified by melt spinning as follows. Individual specimens of about 10 g were remelted in a quartz tube, followed by ejection through an ≈ 0.8 mm diameter orifice with an argon gas over pressure of 35–40 kPa, on to the outer surface of a 150 mm diameter polished copper wheel rotating with a tangential velocity of 25–60 $m\,s^{-1}$. Specimens of the resulting melt-spun ribbons were sealed in evacuated quartz tubes partially filled with argon gas, and were then annealed for 7–45 min at temperatures in the range 320–590 °C.

Samples from each of the as-melt-spun and annealed ribbons were ground from either the top or bottom surface to examine the as-rapidly solidified microstructures near the chilled and unchilled surfaces, respectively. The ground samples were then prepared for transmission electron microscopy (TEM) by conventional jet electropolishing using a 3:1 methanol:nitric acid solution at 15–20 V and − 30 °C. The resulting thin foils were examined in a

Philips CM12 TEM. Samples from each of the as-melt-spun and annealed ribbons were also annealed by continuous heating under argon in a Du Pont 1090 differential thermal analyser fitted with a 910 differential scanning calorimeter (DSC) module.

3. Results

3.1. Solidification microstructure

3.1.1. Effect of alloy composition

To investigate the effect of alloy composition, Al–5, 10 and 15 at % Fe alloys were each melt spun at a wheel speed of 40 m s^{-1}. Fig. 1a–g shows typical bright-field transmission electron micrographs near the chilled and unchilled surfaces in the Al–5, 10 and 15 at % Fe ribbons, respectively.

The microstructure near the chilled surface of Al–5 at % Fe melt spun at 40 m s^{-1} consisted of irregular shaped grains, 0.3–0.5 μm in size, with a fine-scale two-phase structure of the α-Al and microquasicrystalline phases within each grain, as shown in Fig. 1a. The microquasicrystalline phase has been shown previously to consist of nanometre-scale randomly oriented icosahedral particles [12], and when present in a fine-scale cellular network with α-Al, has also been referred to as either a microcellular or microeutectic structure [2, 13]. In the slower cooled region near the unchilled surface, the two-phase structure became coarser, as can be seen in Fig. 1b. Fine cellular networks radiating from near-spherical primary particles of the microquasicrystalline phase such as shown in Fig. 1d were also occasionally observed.

The microstructure near the chilled surface of Al–10 at % Fe melt spun at 40 m s^{-1} consisted again of a two-phase cellular structure of the α-Al and microquasicrystalline phases, as shown in Fig. 1c. A typical selected-area electron diffraction pattern (SADP) from the microquasicrystalline phase is shown in the inset in Fig. 1c, and consisted of spotty rings from α-Al and diffuse rings from the microquasicrystalline phase labelled 1–7. The microstructure near the unchilled surface consisted mainly of ≈ 0.2 μm diameter, near-spherical primary particles of the microquasicrystalline phase and a fine cellular structure of the α-Al and microquasicrystalline phases between the particles, as shown in Fig. 1d. Primary particles of the decagonal phase such as shown in Fig. 1f were also occasionally observed near the unchilled surface.

The microstructure near the chilled surface of Al–15 at % Fe melt spun at 40 m s^{-1} consisted mainly of ≈ 0.5 μm size primary particles of the microquasicrystalline phase, as shown in Fig. 1e. The microstructure near the unchilled surface consisted mainly of particles of the decagonal phase, as shown in Fig. 1f. A typical SADP from one of the decagonal phase particles is shown in the inset in Fig. 1f, exhibiting a two-fold symmetry [$D2_a$] diffraction zone [12].

3.1.2. Effect of cooling rate

To investigate the effect of cooling rate, the Al–10 at % Fe alloy was melt spun at wheel speeds of 60, 40, 25 and 10 m s^{-1}. The cooling rate during melt spinning has been shown to increase proportionally with increasing wheel speed [14–16]. Fig. 2a–f shows typical bright-field transmission electron micrographs near the chilled and unchilled surfaces in the Al–10 at % Fe ribbons melt spun at wheel speeds of 60, 25 and 10 m s^{-1}, respectively. For comparison, the microstructure near the chilled and unchilled surfaces in a ribbon melt spun at 40 m s^{-1} is shown in Fig. 1c and d, respectively.

The microstructure near the chilled surface of Al–10 at % Fe melt spun at 60 m s^{-1} was nearly featureless, as shown in Fig. 2a. A typical SADP from the microquasicrystalline phase is shown in the inset in Fig. 2a, and consisted of spotty rings from α-Al and diffuse rings from the microquasicrystalline phase. Compared with the SADP in Fig. 1c, the strong intensity microquasicrystalline rings 2 and 3 were still clearly visible, but other rings could not be seen clearly. The microstructure near the unchilled surface consisted of a coarser cellular two-phase structure of α-Al and microquasicrystalline phases, as shown in Fig. 2b.

The microstructure near both surfaces of Al–10 at % Fe melt spun at 40 m s^{-1} consisted of a cellular structure of α-Al and microquasicrystalline phases and near-spherical primary particles of the microquasicrystalline phase, as shown in Fig. 1c and d.

The microstructure near the chilled surface of Al–10 at % Fe melt spun at 25 m s^{-1}, consisted of a fine-scale degenerate eutectic of the α-Al and Al_mFe phases, as shown in Fig. 2c. The microstructure near the unchilled surface consisted of a coarser eutectic structure of the α-Al and Al_mFe phases, as shown in Fig. 2d.

The microstructure near the chilled surface of Al–10 at % Fe melt spun at 10 m s^{-1}, consisted of an even coarser degenerate eutectic of the α-Al and Al_mFe phases, as shown in Fig. 2e. The microstructure near the unchilled surface consisted mainly of large primary particles of the Al_mFe phase, as shown in Fig. 2f. Occasional primary particles of the $Al_{13}Fe_4$ phase were also observed near the unchilled surface of Al–10 at % Fe melt spun at 25 and 10 m s^{-1}. The inset in Fig. 2f shows a typical SADP from an Al_mFe phase particle, exhibiting a [$\bar{1}$ 1 0] diffraction zone.

3.2. Decomposition behaviour

3.2.1. Ex situ heat treatment

Fig. 3a shows a bright-field transmission electron micrograph near the chilled surface in an Al–10 at % Fe ribbon melt spun at a wheel speed of 60 m s^{-1} and then annealed at 300 °C for 7 min. The SADP inset in Fig. 3a consists of spotty rings from α-Al and continuous rings from the microquasicrystalline phase. Compared with the SADP before heat treatment shown in Fig. 2a, rings 1 and 4–7 can be discerned clearly, indicating a slight coarsening of the microquasicrystalline phase. The corresponding dark-field image in Fig. 3b was taken using the diffraction region marked with a circle in the SADP in Fig. 3a, and illuminated

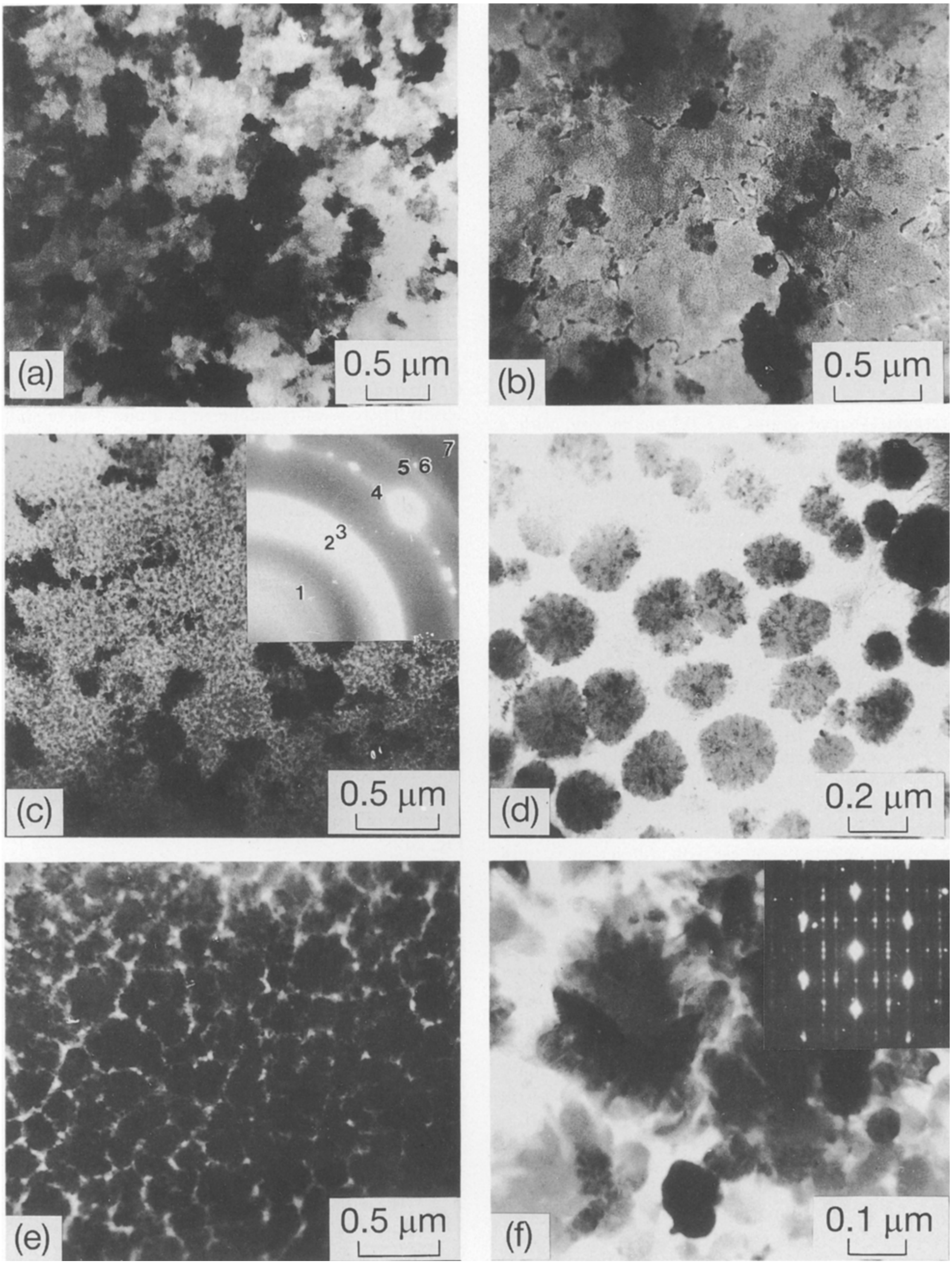

Figure 1 Typical bright-field transmission electron micrographs showing the effect of alloy composition at a wheel speed of 40 m s^{-1}: (a, c, e) near the chilled surfaces of Al–5 at % Fe, Al–10 at % Fe and Al–15 at % Fe, respectively; (b, d, f) near the unchilled surfaces of Al–5 at % Fe, Al–10 at % Fe and Al–15 at % Fe, respectively.

≈ 0.05 μm size aluminium grains, and nanometre-scale particles of the microquasicrystalline phase.

Fig. 4a–c shows a bright-field transmission electron micrograph and corresponding SADPs from an Al–10 at % Fe ribbon melt spun at a wheel speed of 40 m s^{-1} and then annealed at 430 °C for 15 min. After heat treating at the higher temperature of 430 °C, the as-melt-spun microquasicrystalline phase of Fig. 1c and d decomposed completely to form a mixture of the Al_6Fe and Al_mFe phases, as shown in Fig. 4a–c. At the

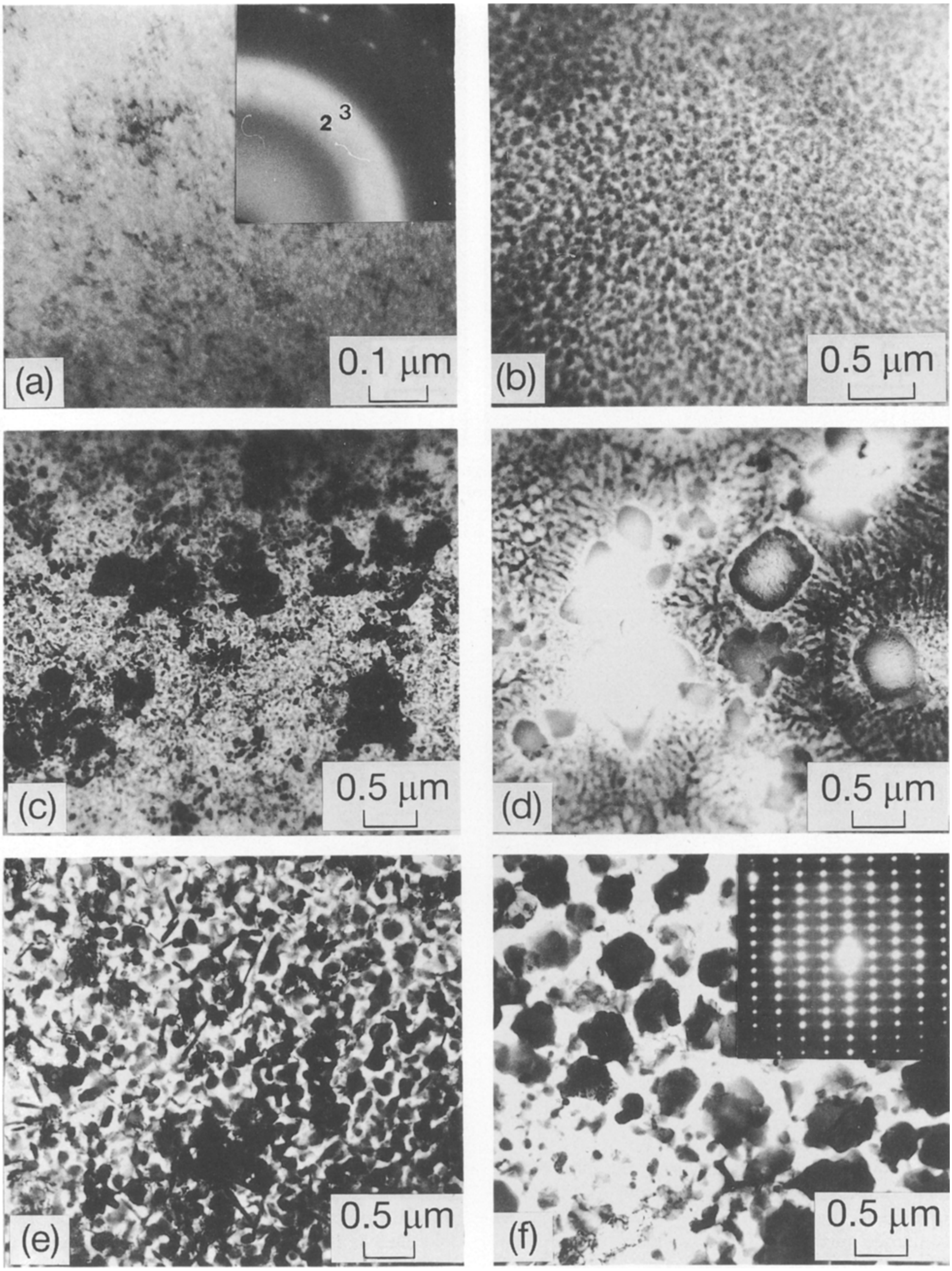

Figure 2 Typical bright-field transmission electron micrographs showing the effect of cooling rate in Al–10 at % Fe: (a, c, e) near the chilled surfaces of ribbons melt spun at wheel speeds of 60, 25 and 10 m s^{-1}, respectively; (b, d, f) near the unchilled surfaces of ribbons melt spun at wheel speeds of 60, 25 and 10 m s^{-1}, respectively.

same time, the occasional primary decagonal particles in the unchilled region were found to decompose to a mixture of decagonal and ten-fold twinned $Al_{13}Fe_4$ phases, as shown in Fig. 5a and b. The SADP in Fig. 5b was taken from the area marked in Fig. 5a, and consisted of a [$D2_a$] zone from the decagonal phase superimposed on the combined [0 0 1], [1 0 0], [1 0 2] and [5 0 4] zones from ten-fold twinned $Al_{13}Fe_4$ [17].

Fig. 6 shows a bright-field transmission electron micrograph of an Al–10 at % Fe ribbon melt spun at a wheel speed of 40 m s^{-1} and then annealed at 590 °C

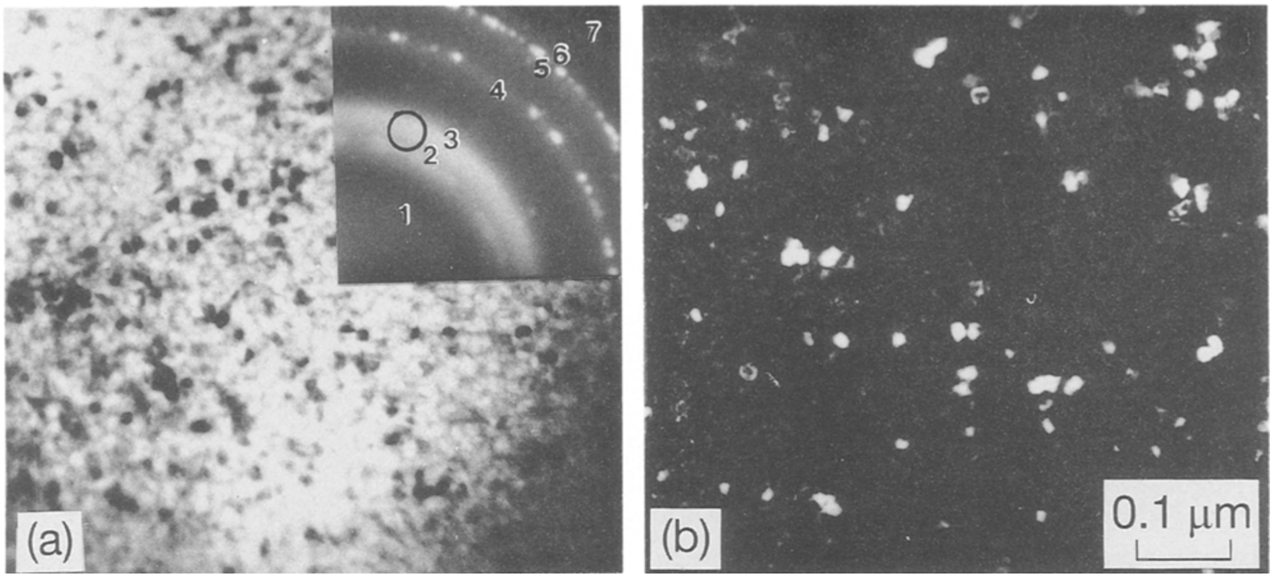

Figure 3 (a) Bright-field transmission electron micrograph of the microquasicrystalline phase in melt spun Al–10 at % Fe (60 m s^{-1}) after annealing at 320 °C for 7 min and corresponding selected-area diffraction pattern consisting of spotty rings from α-Al and continuous rings from the microquasicrystalline phase; (b) dark-field transmission electron micrograph of the same area as in (a) taken from the diffraction region marked with a circle in the selected-area diffraction pattern in (a).

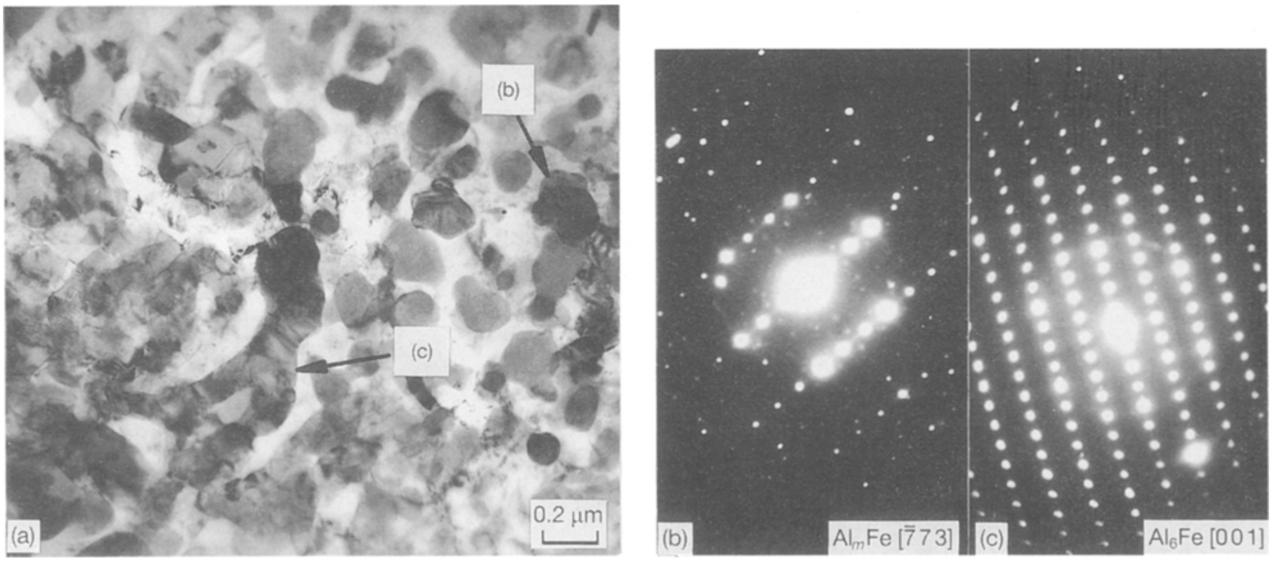

Figure 4 (a) Bright-field transmission electron micrograph showing a mixture of the Al_mFe and Al_6Fe phases in melt-spun Al–10 at % Fe (40 m s^{-1}) after annealing at 430 °C for 15 min; (b, c) selected-area diffraction patterns showing $[\bar{7}\,7\,3]_{Al_mFe}$ and $[0\,0\,1]_{Al_6Fe}$ zones, respectively, from the particles marked (b) and (c) in (a).

for 45 min. After heat treating at the even higher temperature of 590 °C, the Al_6Fe and Al_mFe phases which had precipitated at lower temperatures, decomposed further to form a mixture of α-Al and $Al_{13}Fe_4$ phases, as shown in Fig. 6.

Fig. 7a and b shows bright-field transmission electron micrographs near the chilled and unchilled surfaces of an Al–15 at % Fe ribbon melt spun at a wheel speed of 40 m s^{-1} and then annealed at 480 °C for 15 min. The as-melt-spun microquasicrystalline phase near the chilled zone, such as shown in Fig. 1e, decomposed to form a mixture of the α-Al and Al_mFe phases, as can be seen in Fig. 7a. At the same time, the as-melt-spun decagonal phase near the unchilled surface, such as shown in Fig. 1f, decomposed to form a mixture of α-Al and ten-fold twinned $Al_{13}Fe_4$, as can be seen in Fig. 7b. The inset SADP taken from the marked crystal in Fig. 8b shows superimposed ten-fold twinned [0 1 0] zones.

3.2.2. *In situ* heat treatment

The series of micrographs in Fig. 8 show results obtained by *in situ* TEM heating experiments on Al–10 at % Fe ribbons melt spun at a wheel speed of 40 m s^{-1}. Fig. 8a shows particles of the microquasicrystalline phase, ≈ 0.2 μm in size, and Fig. 8b shows a corresponding SADP consisting of microquasicrystalline rings superimposed on diffraction spots from α-Al. Fig. 8c shows the same area as Fig. 8a immedi-

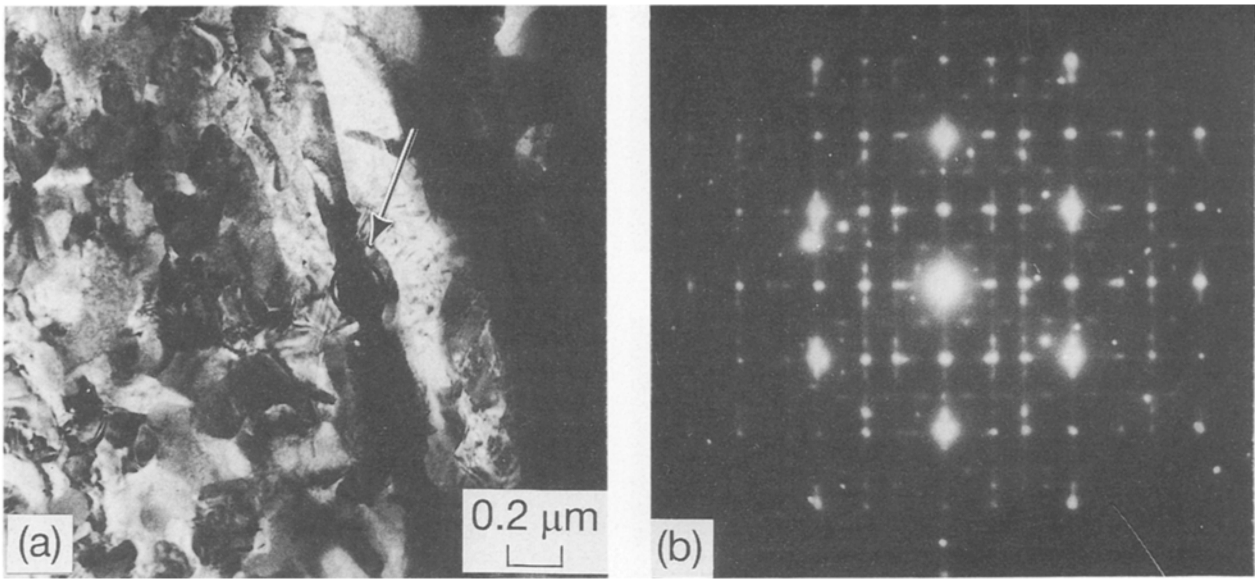

Figure 5 (a) Bright-field transmission electron micrograph showing a decomposing primary decagonal phase particle in melt-spun Al–10 at % Fe (40 m s^{-1}) after annealing at 430 °C for 15 min; (b) selected-area diffraction pattern taken from the particle marked with an arrow in (a) consisting of a [D2$_a$] zone from the decagonal phase superimposed on the combined [0 0 1], [1 0 0], [1 0 2] and [5 0 4] zones from the ten-fold twinned $Al_{13}Fe_4$.

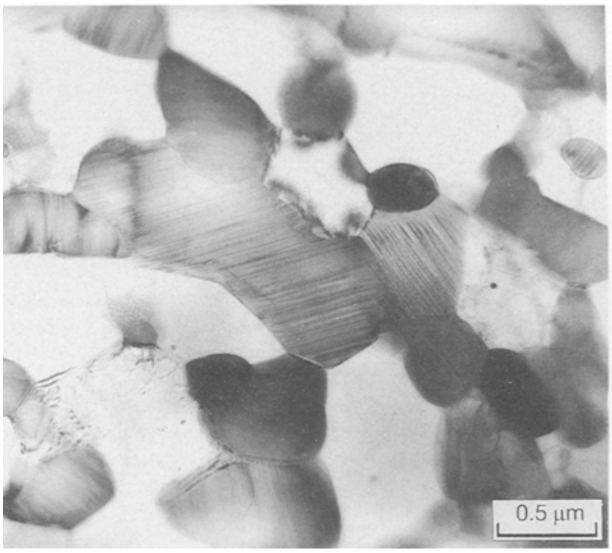

Figure 6 Bright-field transmission electron micrograph showing a mixture of equilibrium α-Al and $Al_{13}Fe_4$ phases in melt-spun Al–10 at % Fe (40 m s^{-1}) after annealing at 590 °C for 45 min.

ately after *in situ* heating up to ≈ 370 °C in the TEM. The particles of the microquasicrystalline phase, marked A and B in Fig. 8a, transformed into two corresponding particles of the Al_mFe phase, marked A and B in Fig. 8c. The SADP in Fig. 8d shows an $[0\,3\,1]_{Al_mFe}$ zone from particle A in Fig. 8c. Fig. 8e shows another particle of the Al_mFe phase after holding at ≈ 370 °C for 1.5 min, and the SADP in Fig. 8f shows a corresponding $[3\,\bar{3}\,1]_{Al_mFe}$ zone. Fig. 8g shows a particle of the Al_6Fe phase which formed after holding at ≈ 370 °C for the longer time of 5 min, and the SADP in Fig. 8h shows a corresponding $[1\,0\,1]_{Al_6Fe}$ zone. After heating up to ≈ 490 °C, $Al_{13}Fe_4$ formed, as shown in the bright-field TEM image and $[0\,0\,1]_{Al_{13}Fe_4}$ zone SADP of Fig. 8i and j, respectively.

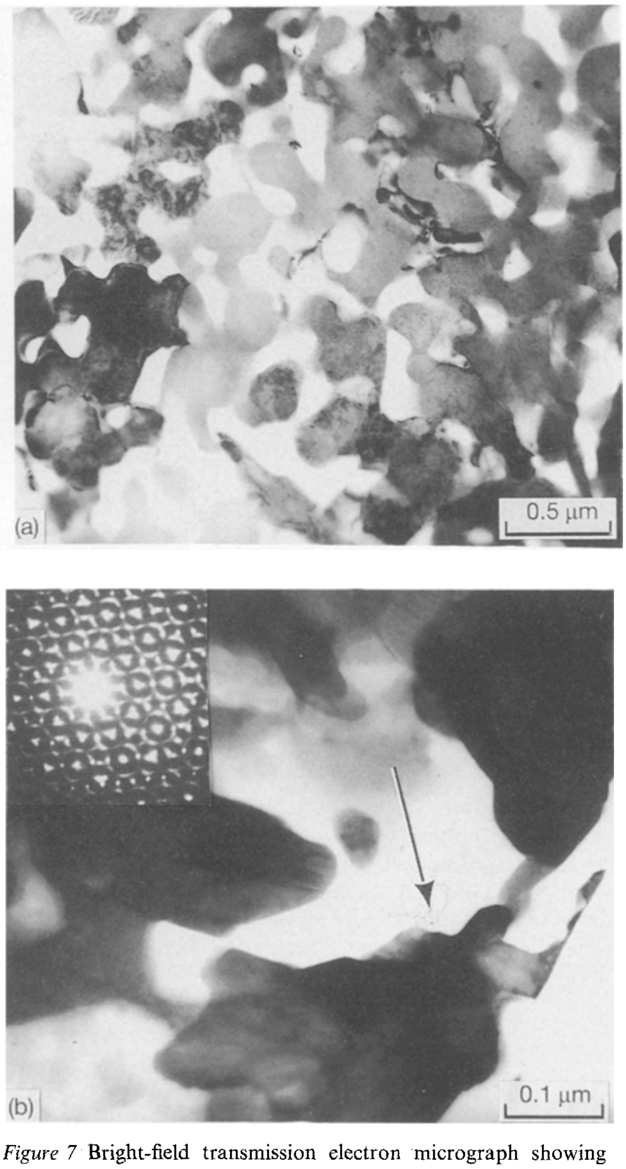

Figure 7 Bright-field transmission electron micrograph showing (a) α-Al and Al_mFe near the chilled surface and (b) α-Al and ten-fold twinned $Al_{13}Fe_4$ near the unchilled surface in melt-spun Al–15 at % Fe (40 m s^{-1}) after annealing at 480 °C for 15 min.

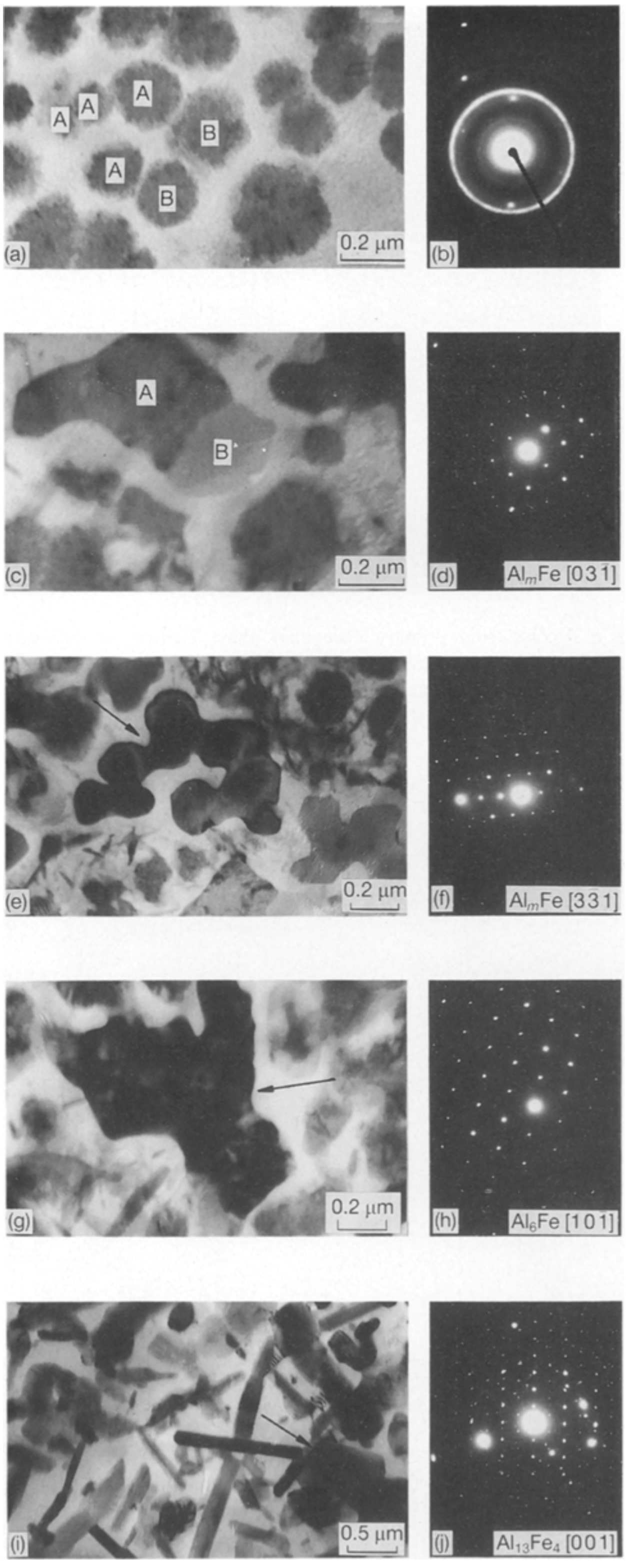

Figure 8 Bright-field transmission electron micrographs and corresponding selected-area diffraction patterns showing microstructural changes during *in situ* heating of as-melt-spun Al–10 at % Fe (40 m s^{-1}) in the TEM: (a, b) as-melt-spun; (c, d) after heating to 370 °C; (e, f) after holding for 1.5 min at 370 °C; (g, h) after holding for 5 min at 370 °C; (i, j) after heating to 490 °C.

3.3. DSC results

Fig. 9a–h shows typical DSC traces from as-melt-spun and annealed treated Al–Fe alloys. Three exothermic peaks, labelled I, II and III, were present in DSC traces from Al–10 at % Fe ribbons melt spun at wheel speeds of 60 and 40 m s^{-1}, as can be seen in Fig. 9a and b, respectively. Peak I appeared over the temperature range 320–360 °C with a peak temperature of 340 °C. At the higher cooling rate corresponding to the higher wheel speed of 60 m s^{-1}, peak I was larger, as can be seen by comparing Fig. 9a and b. Peak I reduced in size or disappeared after annealing at 320 °C for 7 min, as can be seen in Fig. 9c and d. Therefore, peak I, corresponded to the coarsening of icosahedral particle clusters in the microquasicrystalline phase, as shown in Fig. 3. Peak II appeared over the temperature range 340–420 °C with a peak temperature of 390 °C, but disappeared after annealing at 430 °C for 15 min, as can be seen in Fig. 9e and, therefore, corresponded to decomposition of the microquasicrystalline phase into the Al$_m$Fe and Al$_6$Fe, as shown in Fig. 4. Peak III appeared over the temperature range 480–590 °C with a peak temperature of ≈ 550 °C, and corresponded to the decomposition of Al$_m$Fe and Al$_6$Fe and precipitation of Al$_{13}$Fe$_4$, as shown in Fig. 6.

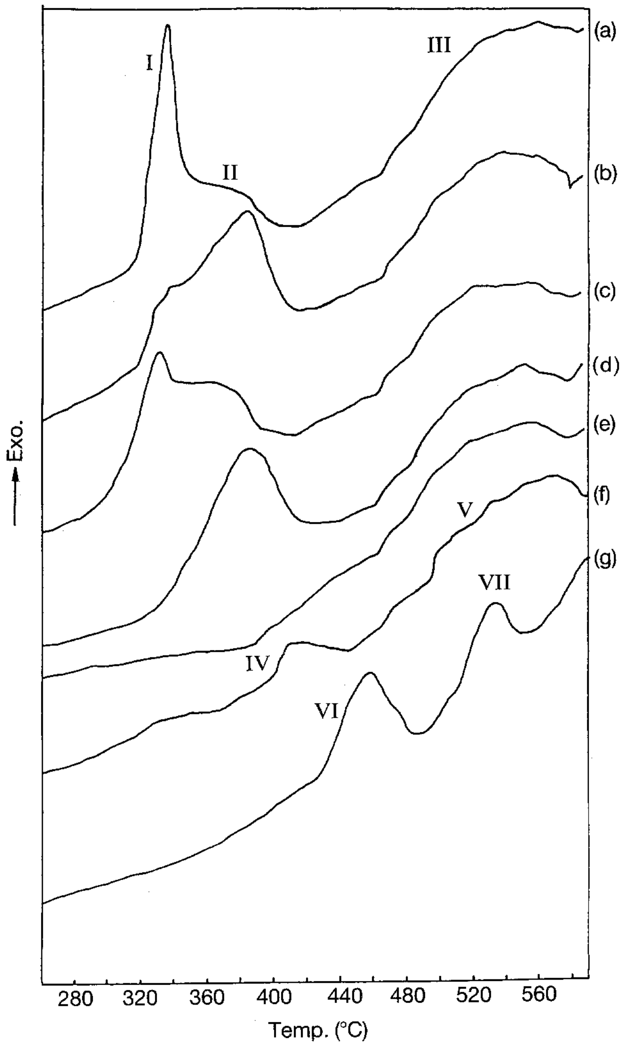

Figure 9 Typical DSC traces from as-melt-spun and annealed Al–Fe alloys: (a) as-melt-spun Al–10 at % Fe (60 m s^{-1}); (b) as-melt-spun Al–10 at % Fe (40 m s^{-1}); (c) melt-spun Al–10 at % Fe (60 m s^{-1}) after annealing at 320 °C for 7 min; (d) melt-spun Al–10 at % Fe (40 m s^{-1}) after annealing at 320 °C for 7 min; (e) melt-spun Al–10 at % Fe (40 m s^{-1}) after annealing at 430 °C for 15 min; (f) as-melt-spun Al–5 at % Fe (40 m s^{-1}); (g) as-melt-spun Al–15 at % Fe (40 m s^{-1}).

Two exothermic peaks, IV and V, were present in DSC traces from Al–5 at % Fe melt spun at a wheel speed of 40 m s^{-1}, as shown in Fig. 9f. The exothermic peak IV appeared over the temperature range 390–450 °C with a peak temperature of $\approx$ 400 °C, and corresponded to decomposition of the microquasicrystalline phase into the $\mathrm{Al}_m\mathrm{Fe}$ and $\mathrm{Al}_6\mathrm{Fe}$ phases. The exothermic peak V appeared over the temperature range 480–560 °C with a peak temperature of $\approx$ 550 °C, and corresponded to decomposition of the $\mathrm{Al}_m\mathrm{Fe}$ and $\mathrm{Al}_6\mathrm{Fe}$ phases and precipitation of the $\mathrm{Al}_{13}\mathrm{Fe}_4$ phase. A small exothermic reaction was also present over the temperature range 310–360 °C. The origin of this exothermic reaction was not clear, but may have corresponded to coarsening of a small amount of icosahedral particle clusters, as in the case of peak I in Fig. 9a and b.

Two exothermic peaks, VI and VII, were present in DSC traces from Al–15 at % Fe melt spun at a wheel speed of 40 m s^{-1}, as shown in Fig. 9g. The exothermic peak VI appeared over the temperature range 430–500 °C with a peak temperature of $\approx$ 450 °C; the exotherm peak VII appeared over the temperature range 510–560 °C with a peak temperature of $\approx$ 530 °C. From the results in Fig. 7a and b, peak VI corresponds to decomposition of the microquasicrystalline phase into the $\mathrm{Al}_m\mathrm{Fe}$ phase, and peak VII corresponds to decomposition of the $\mathrm{Al}_m\mathrm{Fe}$ phase into the $\mathrm{Al}_{13}\mathrm{Fe}_4$ phase, as in the case of peak III in Fig. 9a and b.

4. Discussion

4.1. Solidification microstructure

Rapid solidification of Al–5, 10 and 15 at % Fe alloys result in various types of microstructure depending upon the alloy composition and cooling rate. Table I summarizes the microstructures in as-rapidly solidified Al–Fe alloys as a function of alloy composition and cooling rate. With lower cooling rate at lower wheel speed, the microquasicrystalline phase in the form of primary particles or a fine cellular network is replaced by the $\mathrm{Al}_m\mathrm{Fe}$ phase in the form of primary particles or eutectic with α-Al. With increasing iron content, the microquasicrystalline phase in the form of primary particles or a fine cellular network is replaced with the decagonal phase in the form of primary particles.

TABLE I Dominant Al–Fe phases in as-melt-spun Al–Fe alloys with different alloy compositions and cooling rates

Wheel speed (m s^{-1})	Al–5 at % Fe	Al–10 at % Fe	Al–15 at % Fe
10		Primary $\mathrm{Al}_m\mathrm{Fe}$ + $\mathrm{Al}_m\mathrm{Fe}/\alpha$ eutectic	
25		Primary $\mathrm{Al}_m\mathrm{Fe}$ + $\mathrm{Al}_m\mathrm{Fe}/\alpha$ eutectic	
40	Fine cellular network of MQP/α[a]	Primary MQP + fine cellular network of MQP/α	Primary MQP + primary decagonal phase
60		Fine cellular network of MQP/α	

[a] MQP, microquasicrystalline phase.

4.2. Decomposition behaviour

After annealing, the metastable phases observed in the as-rapidly solidified ribbons decompose into phases with higher stability. In Al–5 and 10 at % Fe the microquasicrystalline phase decomposes into $\mathrm{Al}_m\mathrm{Fe}$ and $\mathrm{Al}_6\mathrm{Fe}$ over the temperature ranges 340–420 and 390–450 °C, respectively. The *in situ* heating results in Fig. 8 show that groups of microquasicrystalline phase particles are replaced by $\mathrm{Al}_m\mathrm{Fe}$ and $\mathrm{Al}_6\mathrm{Fe}$ phase particles. The $\mathrm{Al}_m\mathrm{Fe}$ and $\mathrm{Al}_6\mathrm{Fe}$ phases then decompose into stable $\mathrm{Al}_{13}\mathrm{Fe}_4$ over the temperature ranges 480–590 and 480–560 °C in Al–5 and 10 at % Fe, respectively.

In Al–15 at % Fe the microquasicrystalline phase decomposes into $\mathrm{Al}_m\mathrm{Fe}$ over the temperature range 430–500 °C, and the $\mathrm{Al}_m\mathrm{Fe}$ phase then decomposes into stable $\mathrm{Al}_{13}\mathrm{Fe}_4$ over the temperature range 510–560 °C. Decagonal phase particles transform gradually into stable ten-fold twinned $\mathrm{Al}_{13}\mathrm{Fe}_4$ particles, with a specific orientation relationship as can be seen in Figs 1, 5 and 7.

5. Conclusion

1. Rapid solidification of Al–5, 10 and 15 at % Fe alloys produces a variety of metastable phases: microquasicrystalline, decagonal, $\mathrm{Al}_m\mathrm{Fe}$ and $\mathrm{Al}_6\mathrm{Fe}$, in order of increasing thermodynamic stability.

2. The rapidly solidified microstructure of as-melt-spun Al–Fe alloys depends upon the alloy composition and cooling rate. In Al–10 at % Fe the microquasicrystalline phase is preferred at higher cooling rates, and the $\mathrm{Al}_m\mathrm{Fe}$ phase is preferred at lower cooling rates. The microquasicrystalline and $\mathrm{Al}_m\mathrm{Fe}$ phases are in the form of primary particles of a fine cellular/eutectic structure with α-Al. With increasing iron content, the microquasicrystalline phase in Al–5 and 10 at % Fe is replaced with the decagonal phase in the form of primary particles in Al–15 at % Fe.

3. After annealing at moderate temperatures, the microquasicrystalline phase in Al–5 and 10 at % Fe decomposes into $\mathrm{Al}_m\mathrm{Fe}$ and $\mathrm{Al}_6\mathrm{Fe}$, and the microquasicrystalline phase in Al–15 at % Fe decomposes into $\mathrm{Al}_m\mathrm{Fe}$. After annealing at higher temperatures, the $\mathrm{Al}_m\mathrm{Fe}$, $\mathrm{Al}_6\mathrm{Fe}$ and decagonal phases then decompose into $\mathrm{Al}_{13}\mathrm{Fe}_4$.

References

1. H. JONES, *Mater. Sci. Eng.* **5** (1969/1970) 1.
2. W. J. BOETTINGER, L. BENDERSKY and F. EARLY, *Met. Trans.* **17A** (1986) 781.
3. M. CHANDRASEKAREN, Y. P. LIN, R. VINCENT and G. STANIEK, *Scripta Metall.* **22** (1988) 797.
4. P. J. SHURER, B. KOOPMANO and F. VAN DER WONDE, *Solid State Commun.* **59** (1986) 619.
5. R. M. K. YOUNG and T. W. CLYNE, *Scripta Metall.* **15** (1981) 1211.

6. K. K. FUNG, C. Y. YANG, Y. Q. ZHOU, J. G. ZHAO, W. S. ZHAN and B. C. SHEN, *Phys. Rev. Lett.* **56** (1986) 2060.
7. C. M. ADAM, V. R. V. RAMANAN and D. J. SKINNER, in "Undercooled Alloy Phases", edited by E. W. Collings and C. C. Tioch (AIME, Warrendale, 1986) p. 89.
8. R. A. DUNLAP, D. J. LLOYD, I. A. CHRISTIE, G. STRONIK and Z. M. STADUNIK, *J. Phys. F Met. Phys.* **18** (1988) 1329.
9. I. R. HUGHES and H. JONES, *J. Mater. Sci.* **11** (1976) 1781.
10. C. M. ADAM and L. M. HOGAN, *J. Austral. Inst. Met.* **17** (1972) 81.
11. M. H. JACOBS, A. G. DOGGET and M. J. STOWELL, *J. Mater. Sci.* **9** (1974) 1631.
12. D. H. KIM, PhD thesis, Oxford University, (1989).
13. J. D. FITZ GERALD, R. L. WITHERS, A. M. STEWART and A. CALKA, *Philos. Mag. B* **58** (1988) 15.
14. A. G. GILLEN and B. CANTOR, *Acta Metall.* **33** (1985) 1813.
15. B. BEWLAY and B. CANTOR, *Int. J. Rapid Solid.* **2** (1986) 107.
16. W. T. KIM and B. CANTOR, *Scripta Metall.* **24** (1990) 633.
17. X. D. ZOU, K. K. FUNG and K. H. KUO, *Phys. Rev. B* **35** (1987) 4526.

Received 26 May
and accepted 31 August 1993